Chinese Journal of Chemical Engineering 87 (2025) 229–238

Contents lists available at ScienceDirect

Chinese Journal of Chemical Engineering

journal homepage: www.elsevier.com/locate/CJChE

Full Length Article

Citric acid-modified silicon anode with dual carbon stress modulation for stable lithium storage

Qianqian Fan [1], Jing Wang [1], Zhiyuan Gao [1], Zhenpeng Zhu [1], Xingmei Guo [1], Yuanjun Liu [1], Xiangjun Zheng [1], Zhongyao Duan [1], Qinghong Kong [2], Junhao Zhang [1,*]

[1] School of Environmental and Chemical Engineering, Jiangsu University of Science and Technology, Zhenjiang 212003, China
[2] School of the Environment and Safety Engineering, Jiangsu University, Zhenjiang 212013, China

ARTICLE INFO

Article history:
Received 9 February 2025
Received in revised form
13 May 2025
Accepted 9 June 2025
Available online 22 July 2025

Keywords:
Dual carbon stress modulation
Citric acid
Silicon anodes
Electrochemistry
Volume expansion
Kinetics

ABSTRACT

To effectively enhanced structural stability and cycling performance, a dual carbon protection strategy is proposed to fabricate Si nanoparticles encapsulated in citric acid (CA)-derived inner carbon layer and zeolitic imidazolate framework-67 (ZIF-67) derived outer carbon layer (Si@C-CA@c-ZIF). The results reveal that citric acid-derived carbon facilitates a uniform ZIF-67 coating on the Si surface and serves as the inner carbon precursor to reduce volumetric expansion of Si particles, more importantly, it can enhance the transport of electrons and ions between Si particles and ZIF-67-derived carbon. The ZIF-67-derived outer carbon layer further restricts Si particle expansion and enhances conductivity. Evaluated as anode material for lithium ion batteries, the Si@C-CA@c-ZIF anode demonstrates outstanding lithium storage performance, the high specific capacity is high to 924 $mA \cdot h \cdot g^{-1}$ at 1.0 $A \cdot g^{-1}$ after 10 cycles of activation, and it still maintains a reversible capacity of 703.3 $mA \cdot h \cdot g^{-1}$ after 1000 cycles, along with a capacity retention of 76.1%. This work highlights the effectiveness of the dual carbon framework in addressing the volume expansion and conductivity limitations of Si, with potential applications for other high-capacity anode materials.

1. Introduction

Lithium-ion batteries (LIBs) are pivotal devices for large-scale sustainable energy storage [1]. The anode materials used in commercial LIBs primarily consist of graphite, which accommodates lithium ions and exhibits a theoretical capacity of 372 $mA \cdot h \cdot g^{-1}$. However, this capacity is insufficient to meet the market demand for high-energy-density storage solutions [2,3]. Consequently, it is imperative to develop novel anode materials that offer high capacity, low charge/discharge potentials, and reduced production costs. Silicon (Si), with a theoretical specific capacity exceeding 4000 $mA \cdot h \cdot g^{-1}$, presents a promising alternative anode material for LIBs. Furthermore, Si exhibits a low voltage platform ($\approx$0.4 V *vs.* Li/Li^+), abundant reserves, and low cost, making it suitable for next-generation LIBs [4]. Nevertheless, Si undergoes significant volumetric expansion and contraction during lithiation and delithiation, resulting in rapid capacity degradation [5,6]. Additionally, Si displays extremely poor electrical conductivity, further impeding its practical application in LIBs [7,8].

The incorporation of Si with conductive carbon is a compromise yet effective strategy to mitigate volumetric expansion of Si and improve the overall conductivity, thereby improving its cycling stability [9,10]. Metal-organic frameworks (MOFs) are increasingly recognized as promising multifunctional carbon-derived materials for improving the conductivity of Si anodes, owing to their high specific surface area and abundant lithium-storage active sites [11]. Furthermore, MOF-derived carbon materials exhibit tunable porous structures that facilitate the uniform distribution of electroactive materials and promote rapid Li^+ migration [12]. For example, Gao *et al.* [13] reported an *in situ* method for coating Si nanoparticles with a MOF-derived carbon shell, creating a robust interface that minimizes unnecessary exposure and significantly enhances cycling stability. In addition to MOFs, citric acid (CA), naturally abundant and cost-effective organic acid, has emerged as a competitive organic carbon source. Compared to more complex inorganic carbon sources such as carbon nanotubes and graphene,

* Corresponding author.
E-mail address: jhzhang6@just.edu.cn (J. Zhang).

https://doi.org/10.1016/j.cjche.2025.06.012

CA-derived carbon offers advantages in affordability and environmental sustainability. Furthermore, the carboxyl groups of CA can undergo esterification with the hydroxyl groups on the nano-Si surface, forming robust hydrogen bonds that effectively mitigate the severe agglomeration of Si nanoparticles and uncontrolled growth of the SEI, thereby enhancing the cycling stability of Si anode [14]. Upon thermal treatment, CA decomposes into a conductive carbon coating that uniformly envelops Si particles, improving their conductivity and reducing volumetric expansion, thus enhancing rate capability and capacity retention [15]. However, both MOF- and CA-derived single carbon coatings exhibit limited mechanical strength, risking structural degradation during prolonged cycling and compromising the long-term stability of Si anodes. Additionally, fully encapsulating Si nanoparticles with single carbon coating layer remains challenging. Incomplete coating can result in an unstable SEI and significant capacity degradation. It is hypothesized that the construction of Si anode materials with dual carbon coating layers would lead to further improvement.

Inspired by previous research, novel Si composite with dual carbon layer derived from CA and ZIF-67 (Si@C-CA@c-ZIF) was fabricated by two-step coating and calcination strategy. The Si@C-CA@c-ZIF exhibited efficient electron transport pathways and constrained volume changes. Specifically, CA served as the inner carbon precursor, mitigating Si pulverization and volumetric expansion while facilitating a uniform ZIF-67 coating on the Si surface. Additionally, the MOF-derived outer carbon layer further restricted Si particle expansion and enhanced electrode conductivity. Evaluated as anode material for LIBs, the high specific capacity of Si@C-CA@c-ZIF anode was 924 $mA \cdot h \cdot g^{-1}$ at 1.0 $A \cdot g^{-1}$ after 10 cycles of activation, and it still held a reversible capacity of 703.3 $mA \cdot h \cdot g^{-1}$ after 1000 cycles, with a capacity retention rate of 76.1%. Even at 10 $A \cdot g^{-1}$, the reversible capacity still reached 300.9 mA $h \cdot g^{-1}$. The outstanding cycling stability is mainly attributed to the cooperative protection of the dual carbon layers. In particular, the citric acid-derived carbon layer alleviates the stress generated by silicon during the charging and discharge process, more importantly, enhances the transport of electrons and ions between silicon and ZIF-67-derived carbon.

2. Materials and Methods

2.1. Materials

All the reagents were purchased from Sinopharm Chemical Reagent Co., Ltd, and used as received without any purification.

2.2. Preparation of Si@C-CA

Commercial Si nanoparticles (Si NPs, ~80 nm) and CA were mixed in anhydrous ethanol and treated with ultrasound for 2 h. The mass ratios of Si to CA were 1:1.5, 1:2.5, and 1:3. The Si and CA mixed suspensions were dried at 80 °C in a vacuum oven and further annealed at 800 °C for 2 h under Ar atmosphere. For the preparation of Si@C-Pitch and Si@C-Sucrose samples, CA was replaced directly by pitch and sucrose, respectively. The mass ratios of Si to these organic carbon sources (CA, pitch, sucrose) were both 1:2.5.

2.3. Preparation of Si@C-CA@c-ZIF

0.1 g Si@C-CA nanoparticles were uniformly dispersed in a polyethylenepyrrolidone (PVP) solution (0.6 g PVP in 50 ml ethanol). The obtained solution was subjected to ultrasonic treatment for 2 h, then stirred for 12 h. After centrifugation, the Si@C-CA@PVP was obtained, which was re-dispersed in 100 ml methanol, and 2.7 g 2-methylimidazole was added to produce solution A. Solution B was formed by dissolving 2.5 g $Co(NO_3)_2 \cdot H_2O$ in 100 ml methanol. Solution B was quickly injected into solution A to form a mixed solution, which was transferred to a 300 ml Teflon-lined stainless steel autoclave and treated for 4 h at 120 °C. After cooling to ambient temperature, the precipitates were washed with ethanol, and dried under vacuum for 12 h. Finally, the Si@C-CA@c-ZIF composites were obtained by carbonizing under an Ar/H_2 mixture (V_{Ar}: V_{H2} = 95%: 5%) at 800 °C for 3 h. The Si@C-Pitch@c-ZIF and Si@C-Sucrose@c-ZIF were synthesized in the same manner, except that the Si@C-CA nanoparticles were replaced by Si@C-Pitch and Si@C-Sucrose nanoparticles, respectively.

2.4. Materials characterization

The surface morphology and structure of Si and Si@C-CA@c-ZIF composites, as well as Si and Si@C-CA@c-ZIF anodes before and after cycling, were analyzed using scanning electron microscope (SEM, ZEISS Merlin type) and transmission electron microscope (TEM, JEM2100F). X-ray diffraction (XRD-6000, Cu target, $\lambda = 0.15418$ nm, scan angle 10°–80°, sweep speed 5 (°)·min^{-1}) was employed to analyze the phases of Si and Si@C-CA@c-ZIF samples. X-ray photoelectron spectroscopy (XPS, AXIS UltraDLD) was conducted to investigate the elemental composition, chemical bonding, and atomic valence states of the samples. Carbon content was analyzed using a thermogravimetric method (TGA, TA Instruments, Q50), under an air atmosphere at a heating rate of 10 °C·min^{-1}, ranging from 25°C to 850 °C.

2.5. Electrochemical measurement

The working electrode was prepared by mixing active materials (Si, Si@C-CA@c-ZIF, Si@C-Pitch@c-ZIF, or Si@C-Sucrose@c-ZIF), carbon black (Super P), and sodium carboxymethyl cellulose (CMC) in a ratio of 7:2:1 with deionized water, followed by continuous stirring for 12 h. The slurry was then spread onto pure copper foil and dried overnight at 80 °C under vacuum. The mass loading of active materials in the electrode was approximately 0.9–1.1 $mg \cdot cm^{-2}$. Li foil was used as the counter electrode, and Celgard 2400 served as the separator. The electrolyte consisted of 1 $mol \cdot L^{-1}$ lithium hexafluorophosphate ($LiPF_6$) dissolved in a mixture of ethylene carbonate (EC) and dimethyl carbonate (DEC) at a 1:1 vol ratio. Cells were galvanostatically cycled on a LAND battery cycler (LAND CT2001A) at different specific currents between 0.01 and 3.0 V. Cyclic voltammetry (CV) was performed using a CHI760E electrochemical workstation, with the potential swept from open circuit voltage to 3.0 V and then cycled between 0.01 and 3.0 V at a scanning rate of 0.02 $mV \cdot s^{-1}$. Electrochemical impedance spectroscopy (EIS) tests were conducted using the same workstation in the frequency range of 1 MHz to 0.1 Hz with an amplitude of 5 mV.

3. Results and Discussion

The synthesis strategy for Si@C-CA@c-ZIF is schematically illustrated in Fig. 1(a). Initially, Si NPs are modified with CA to form Si@CA, where CA serves as both dispersing agent and carbon precursor for the inner carbon layer. Subsequently, Si@CA is annealed in Ar atmosphere to produce Si@C-CA nanoparticles. The final step involves calcining Si@C-CA@ZIF-67 in Ar, resulting in the formation of the outer carbon coating derived from ZIF-67 on the Si@C-CA surface, thereby producing Si@C-CA@c-ZIF-67. Notably, the strong interactions between the hydroxyl (—OH) groups on the Si surface and the carboxyl (—COOH) groups of CA are crucial

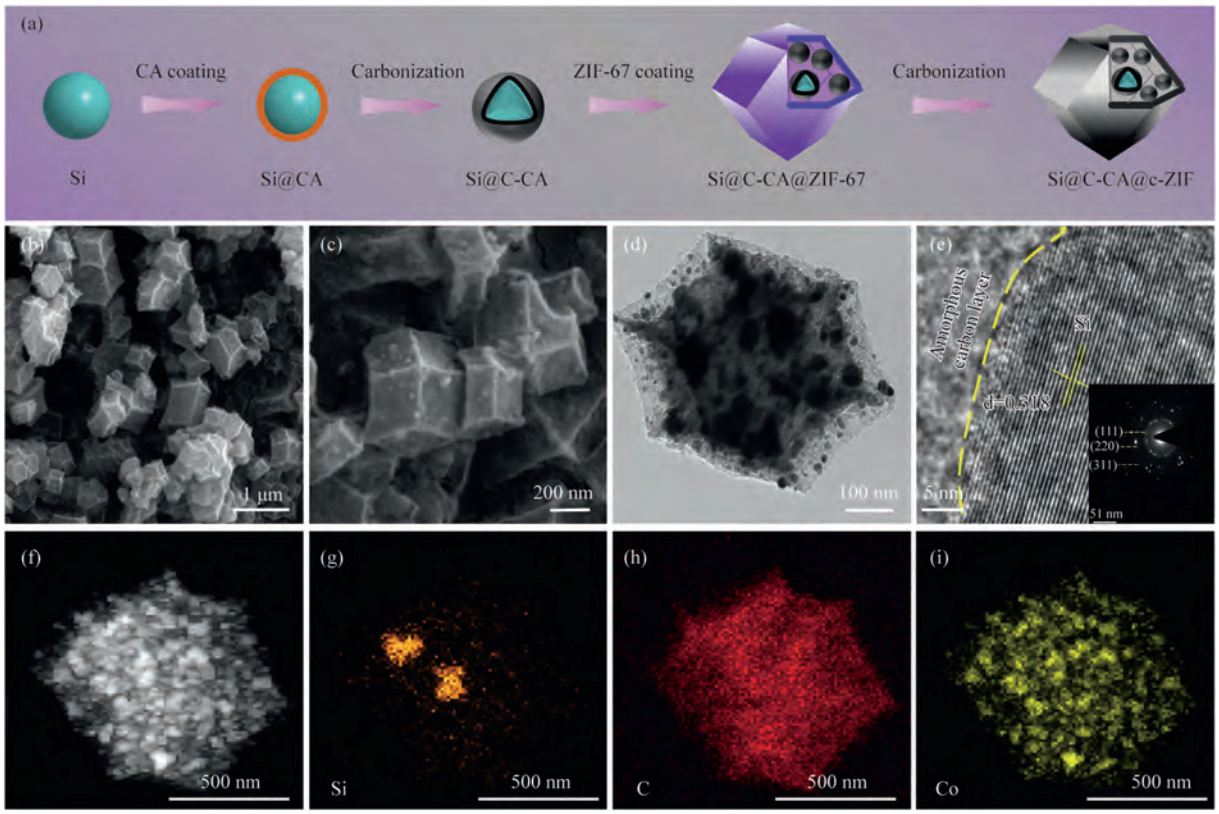

Fig. 1. (a) Schematic illustration of the synthesis of Si@C-CA@c-ZIF. (b, c) SEM images and (d, e) TEM and HRTEM images of Si@C-CA@c-ZIF. and the insets show the corresponding SAED pattern. (f–i) STEM and elemental mapping images of Si@C-CA@c-ZIF.

for reducing nanoparticle aggregation, significantly enhancing the efficacy of the ZIF-67-derived outer carbon layer coating. The SEM and TEM images reveal that Si@C-CA@c-ZIF-67 exhibits uniform polyhedral structure with rough surface and an average dimension of approximately 0.5 μm, akin to that of ZIF-67 (Fig. 1(b) and (c)). The accumulation of Co^{2+} in a high-temperature inert atmosphere results in the formation of cobalt nanoparticles, contributing to the rough surface of carbonized ZIF-67. Importantly, no aggregated Si NPs are observed on the surface of Si@C-CA@c-ZIF-67, attributed to the hydrogen bonding interactions between the nano-Si surface and CA, which promote nanoparticle dispersion and effective encapsulation within ZIF-67. TEM analysis (Fig. 1(d)) further demonstrates that Si@C-CA nanoparticles are uniformly embedded within ZIF-67-derived carbon shell, forming compact composite structure. High-resolution TEM (HRTEM) images reveal that the Si NPs are coated with thin amorphous carbon layer derived from CA (Fig. 1(e)), with a distinct lattice fringe corresponding to the (1 1 1) plane of Si, exhibiting a planar spacing of 0.318 nm [16]. The selected area electron diffraction (SAED) pattern confirms the presence of polycrystalline Si, characterized by bright spots and distinct diffraction rings corresponding to the (1 1 1), (2 2 0), and (3 1 1) planes [12]. Scanning TEM (STEM) and elemental mapping images in Fig. 1(f)–(i) reveal the anticipated distribution of Si, C and Co. Notably, C and Co are uniformly distributed within the carbon shell, while Si is exclusively situated at the core of carbon polyhedron, confirming the encapsulation of Si@C-CA nanoparticles. Additionally, the Si@C-CA particles and flexible carbon shell derived from c-ZIF maintain a gap that accommodates the substantial volumetric changes of Si particles. The amorphous carbon layer on the Si surface from CA pyrolysis further mitigates expansion and enhances the conductivity of Si. The specific surface area changes of Si/C composites after carbon coating were also revealed through nitrogen adsorption/desorption measurement (Fig. S1, Suuplementary Material). The Si@C-CA@c-ZIF composite exhibits larger specific surface area and total pore volume compared to both Si@C-CA and Si@c-ZIF, which can be attributed to the synergistic effects of the dual carbon coating strategy.

The crystal phases of Si@C-CA@c-ZIF were analyzed *via* X-ray diffraction (XRD). As shown in Fig. 2(a), Si@C-CA@c-ZIF exhibits diffraction peaks at 28.3°, 47.2°, 56.0°, 69.0°, and 76.3°, corresponding to the (1 1 1), (2 2 0), (3 1 1), (4 0 0), and (3 3 1) crystallographic planes of Si, respectively, confirming the retention of the original crystalline phases even after calcination at 800 °C [17]. Additional peaks at 44.2°, 51.5°, and 75.9° are attributed to cobalt crystals (JCPDS No. 15-0806) [18]. The organic components of CA and ZIF-67 transform into amorphous conductive carbon shells post-annealing. Fig. 2(b) displays the thermal gravimetric (TG) curve of Si@C-CA@c-ZIF under an air atmosphere. The initial mass loss observed between 0 °C and 100 °C is attributed to moisture absorption. A significant mass loss occurring between 278 °C and 320 °C corresponds to the combustion of carbon in Si@C-CA@c-ZIF. The sharp transition at approximately 317 °C is primarily ascribed to the oxidation of cobalt nanoparticles upon exposure to air, coupled with further combustion of carbon. The cobalt nanoparticle content is quantified at approximately 33.2% (mass) using inductively coupled plasma (ICP) spectroscopy. Based on these findings, the silicon content in Si@C-CA@c-ZIF composite is calculated to be 26.0% (mass). Furthermore, the Si content in Si@C-Pitch@c-ZIF and Si@C-Sucrose@c-ZIF were also evaluated through TG curves (Fig. S2). The silicon contents in Si@C-Pitch@c-ZIF and Si@C-Sucrose@c-ZIF samples are determined to be 24.6% and 27.7%

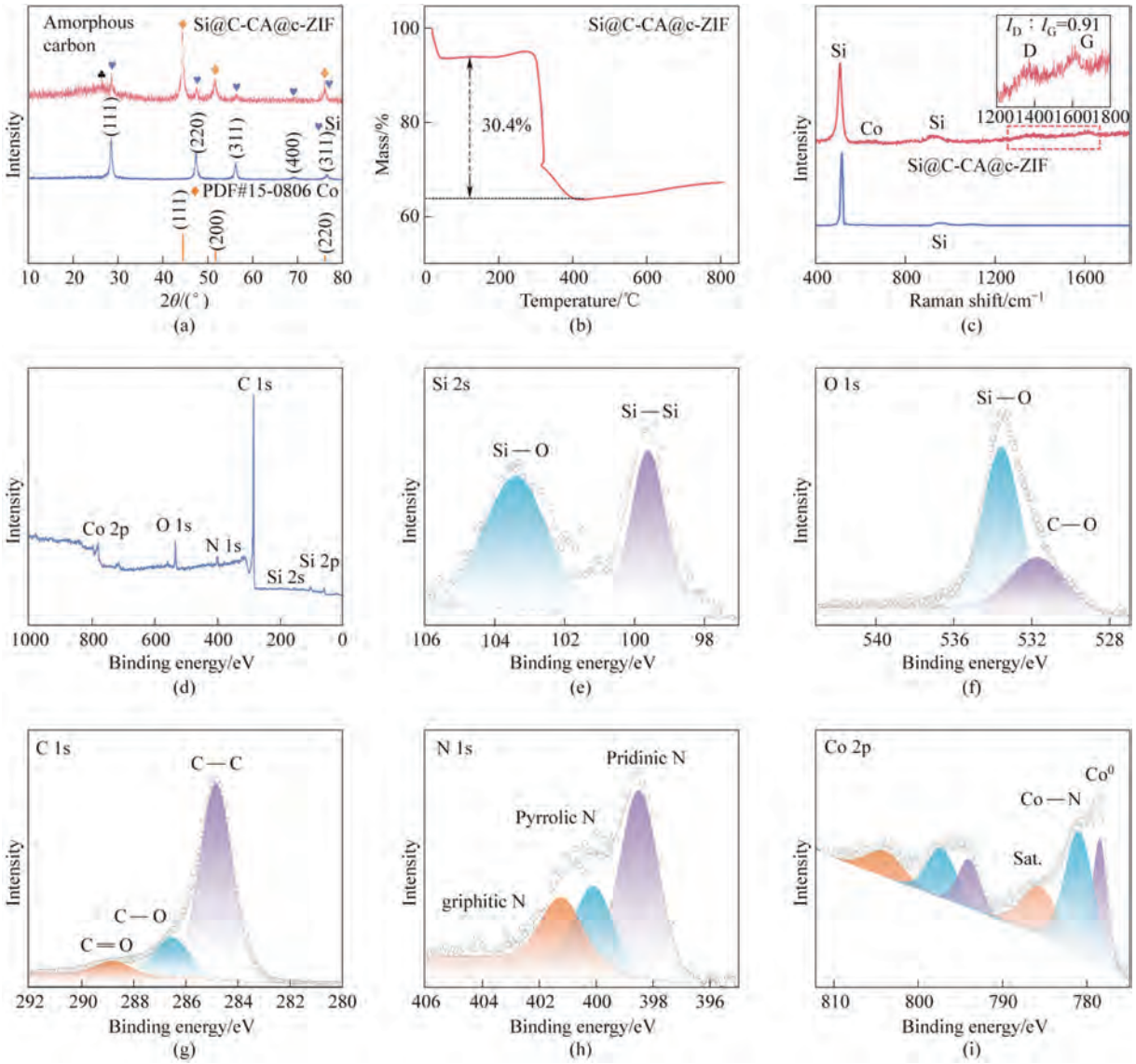

Fig. 2. (a) XRD patterns of Si@C-CA@c-ZIF and bare Si NPs. (b) TG analysis of Si@C-CA@c-ZIF under air conditions. (c) Raman spectra of Si@C-CA@c-ZIF and Si NPs. (d) XPS survey spectrum and high-resolution XPS spectra of (e) Si 2p, (f) O 1s, (g) C 1s, (h) N 1s, and (i) Co 2p.

(mass), respectively, which are in close agreement with the silicon content of the target Si@C-CA@c-ZIF. Fig. 2(c) presents the Raman spectrum of Si@C-CA@c-ZIF, revealing distinct peaks at around 1339 cm^{-1} and 1595 cm^{-1}, which correspond to the D and G bands of carbon derived from CA and ZIF-67 [19]. The I_D/I_G ratio of 0.91 reflects high graphitization and excellent conductivity, facilitating rapid transport of electrons and Li^+. Characteristic peaks of crystalline Si at around 513 cm^{-1} and 945 cm^{-1} further confirm the stability of Si nanoparticles during heat treatment [20]. Additionally, a weak peak for cobalt at approximately 684 cm^{-1} in the Si@C-CA@c-ZIF corroborates the XRD results [21]. As illustrated in Fig. 2(d), the full XPS spectrum of Si@C-CA@c-ZIF reveals the presence of C, N, Si, Co and O, corroborating the elemental mapping results. Notably, the weak Si characteristic peak indicates that Si nanoparticles are encapsulated by the dual carbon shell derived from CA and ZIF-67, with the peak near 99.5 eV corresponding to elemental Si (Si—Si) [14]. The peaks of Si 2p at higher binding energies (103.3 eV) are ascribed to Si in oxidized species of Si (Si—O), which probably derives from the oxidation of a small amount of Si nanoparticles surfaces (Fig. 2(e)) [22]. The Si—O bond is further supported by a peak at about 533.4 eV in the O 1s spectrum (Fig. 2(f)) [20]. In the C 1s XPS spectrum (Fig. 2(g)), the peaks at 284.8, 286.6, and 288.7 eV correspond to the C—C, C—N, and C=O, respectively [23]. The high-resolution N 1s spectrum (Fig. 2(h)) displays peaks at 398.6, 400.0, and 401.2 eV, associated with pyridinic N, pyrrolic N, and graphitic N, respectively [24]. For the Co 2p XPS spectrum (Fig. 2(i)), peaks at 778.5 and 794.1 eV indicate the presence of Co^0, while peaks at 780.9 and 797.2 eV correspond to Co^{2+}, likely arising from surface oxidation of metallic cobalt [25]. The presence of Co and its oxides may inhibit the agglomeration of Si nanoparticles by forming cobalt silicides during carbonization process. These silicides act as physical barrier, restricting Si particle movement and ensuring their uniform distribution [26]. Cobalt also facilitates the graphitization of carbon derived from ZIF-67 by lowering the activation energy required for carbon atoms to reorganize into graphitic domains, thus catalyzing the transformation of amorphous carbon into more ordered graphitic structure [27]. The graphitic carbon

enhances the electrical conductivity and mechanical strength of carbon matrix, which is conducive to improving the overall performance of Si anode material [13]. Moreover, several studies have reported that the inclusion of Co in composites helps to stabilize the electrode structure and enhances the electronic conductivity, which contributes to higher initial Coulombic efficiency (ICE) and better cycling stability [28]. Co can also facilitate the formation of more stable solid electrolyte interface (SEI), further improving the long-term cycling performance [29].

The electrochemical performance of Si@C-CA@c-ZIF was first evaluated using CV. As illustrated in Fig. 3(a)—a cathodic peak appears around 1.2 V during the initial cycle, which is attributed to electrolyte decomposition that forms a SEI film [12]. The sharp cathodic peak at 0.02 V in the first cycle is due to the lithiation of crystalline Si [30]. In the subsequent reduction process, a new cathodic peak at approximately 0.19 V corresponds to the alloy formation from Si to the Li_xSi_y phase [31]. The anodic peaks observed at 0.35 V and 0.51 V are associated with the transformation of Li_xSi_y alloy into amorphous Si [32]. Furthermore, the current intensities of cathodic and anodic peaks gradually increased during subsequent cycles, indicating enhanced activation of Si for reaction with Li^+. Additionally, although the peaks corresponding to crystalline Co consistently appear in the XRD patterns (Fig. 2(a)), no distinct peaks associated with the lithiation/delithiation reactions of Co are observed in the CV curves. This indicates that the metallic Co in Si@C-CA@c-ZIF is electrochemically inactive, which have been verified by previous studies [33]. The galvanostatic charge-discharge (GCD) profiles of Si@C-

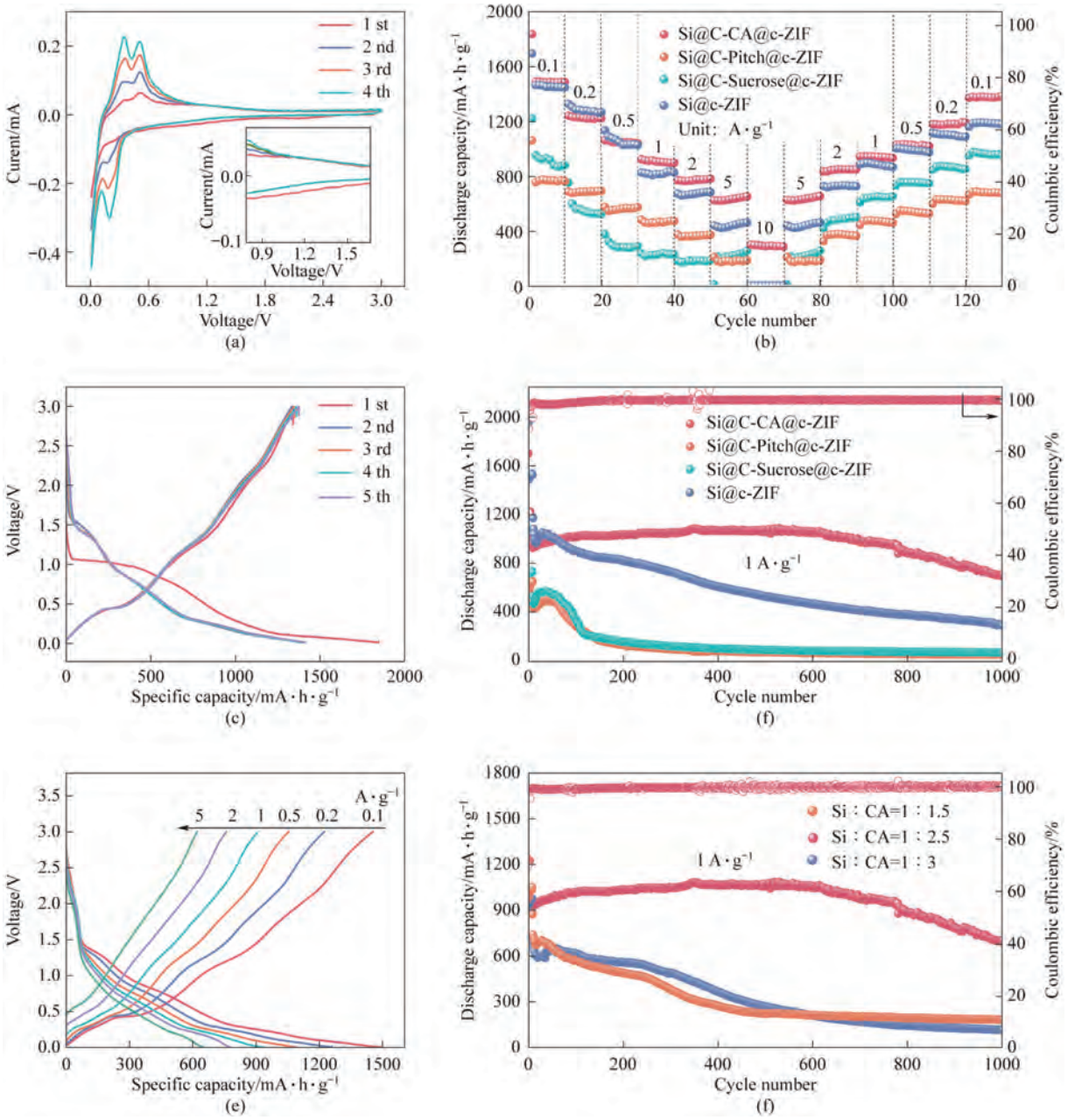

Fig. 3. (a) CV curves of Si@C-CA@c-ZIF anode at 0.1 $mV \cdot s^{-1}$, the inset shows local amplification of CV curves of Si@C-CA@c-ZIF anode. (b) The GCD curves of Si@C-CA@c-ZIF anode in the first five cycles. (c) The GCD curves of Si@C-CA@c-ZIF anode at different current densities. (d) Rate performance and (e) long cycling performance of different anodes at 1.0 $A \cdot g^{-1}$. (f) The cycling performance of Si@C-CA@c-ZIF anodes with varying molar ratios of Si to CA at 1.0 $A \cdot g^{-1}$.

CA@c-ZIF for the first five cycles at 0.1 $A \cdot g^{-1}$ are shown in Fig. 3(b). A pronounced discharge plateau around 0.1 V is observed during the first discharge cycle, corresponding to the lithiation reaction from Si to Li_xSi_y. The charge plateaus between 0.2 V and 0.6 V during the charging process align well with the delithiation of Li_xSi_y back to Si, corroborating the CV results. The charge-discharge profiles for the subsequent four cycles exhibits good overlap, indicating a highly reversible lithiation-delithiation process for Si@C-CA@c-ZIF anode.

To evaluate the rate capability of Si@C-CA@c-ZIF anode, Fig. 3(c) shows the GCD profiles from 0.1 to 5 $A \cdot g^{-1}$. The results indicate that the voltage profiles at elevated current densities exhibit minimal variation, indicating stable rate performance of the Si@C-CA@c-ZIF anode. Furthermore, the Si@C-CA@c-ZIF anode delivers reversible discharge capacities of 1496, 1248.5, 1068.9, 927.7, 773.2, and 655.2 $mA \cdot h \cdot g^{-1}$ at 0.1, 0.2, 0.5, 1, 2, and 5 $A \cdot g^{-1}$, respectively, significantly surpassing those of and Si@c-ZIF anodes (Fig. 3(d)). At a higher current density of 10.0 $A \cdot g^{-1}$, Si@C-CA@c-ZIF anode maintained a commendable specific capacity of 300.9 $mA \cdot h \cdot g^{-1}$, whereas the specific capacities of the other anodes dramatically decreased to nearly 0 $mA \cdot h \cdot g^{-1}$. Additionally, after multiple rate cycles, the reversible capacity of Si@C-CA@c-ZIF anode recovers to 1380.5 $mA \cdot h \cdot g^{-1}$ at 0.1 $A \cdot g^{-1}$. As illustrated in Fig. 3(e), the Si@C-CA@c-ZIF anode is activated after 10 cycles exhibits a stable reversible capacity of 703.3 $mA \cdot h \cdot g^{-1}$ at 1 $A \cdot g^{-1}$ after 1000 cycles with, with a capacity retention of 76.1%, significantly exceeding those of Si@C-Pitch@c-ZIF (45.1 $mA \cdot h \cdot g^{-1}$, 9.4%), Si@C-Sucrose@c-ZIF (60.4 $mA \cdot h \cdot g^{-1}$, 11.5%), and Si@c-ZIF (281.2 $mA \cdot h \cdot g^{-1}$, 24.0%) and Si@C-CA (154.2 $mA \cdot h \cdot g^{-1}$, 16.3%) (Fig. S3). These results unequivocally confirm that the CA-derived inner amorphous carbon layer is pivotal for enhancing the electrochemical performance of Si based anodes, distinguishing it as the most effective carbon source among pitch and sucrose. These results unequivocally confirm that the CA-derived inner amorphous carbon layer is pivotal for enhancing the electrochemical performance of Si/C anodes, distinguishing it as the most effective carbon source among pitch and sucrose. The enhanced electrochemical performance of CA compared to pitch and sucrose in Si anodes can be attributed to its distinctive chemical structure and reactivity during the synthesis process. Unlike pitch and sucrose, CA contains carboxyl groups, which facilitate strong interactions with Si nanoparticles, thereby reducing Si nanoparticle aggregation, significantly enhancing the efficacy of ZIF-67-derived outer carbon layer coating and improving the structural integrity of Si-based anode [34]. During carbonization, CA promotes the formation of uniform and stable inner carbon matrix, effectively mitigating volume expansion and contraction of Si anode during cycling. In contrast, pitch often forms larger, more rigid carbon networks, which are less effective in accommodating the volume changes of Si. Sucrose, while yielding carbon materials, does not form an optimal network of interconnected carbons, thus providing inadequate mechanical support for Si nanoparticles. Additionally, CA-derived carbon exhibits a higher degree of graphitization, leading to improved electrical conductivity, which further enhances electrochemical performance by facilitating charge transport [35]. Thus, the unique chemical and structural properties of CA significantly contribute to the superior electrochemical performance of Si-based anodes. Compared to the high-performance silicon-carbon-based anodes reported in Table S2, although the discharge capacity and cycling stability of Si@C-CA@c-ZIF anode do not yet reach the current optimal levels, its core value lies in the breakthrough of long-term cycling stability through the dual carbon synergistic protection mechanism. By constructing a flexible buffer with CA-derived inner carbon layer and a rigid conductive network with ZIF-67-derived outer carbon layer, the anode retains 76.1% of its initial capacity after 1000 cycles, which is significantly superior to most single carbon-layer coating systems. This strategy of combining rigid and flexible interfaces offers a new pathway to address the volumetric expansion issue of silicon-based materials.

The optimal ratio between Si and CA was further explored by analyzing the cycling stability of a series of Si@C-CA@c-ZIF anodes. As illustrated in Fig. 3(f), the Si@C-CA@c-ZIF anodes with Si-to-CA molar ratios of 1:1.5, 1:2.5, and 1:3 (denoted as Si:CA = 1:1.5, Si:CA = 1:2.5, and Si:CA = 1:3) exhibit different discharge capacities. For the anode with Si:CA = 1:2.5, the Si@C-CA@c-ZIF anode shows the beset specific capacity of 924 $mA \cdot h \cdot g^{-1}$ after the initial 10 cycles, which remained stable at 703.3 $mA \cdot h \cdot g^{-1}$ after 1000 cycles, yielding a capacity retention of 76.1%. These values were significantly higher than those of the anodes with Si:CA = 1:1.5 (181.5 $mA \cdot h \cdot g^{-1}$, 14.7%) and Si:CA = 1:3 (114.2 $mA \cdot h \cdot g^{-1}$, 9.3%). The result suggests that the optimal Si-to-CA ratio is 1:2.5 due to the superior dispersion of CA-modified Si nanoparticles under this condition, which effectively facilitates the uniform coating of ZIF-67 on the surface of Si NPs. The SEM images of Si@C-CA@c-ZIF samples with Si:CA ratios of 1:1.5 and 1:3 were presented in Fig. S5. Compared to the Si@C-CA@c-ZIF composite with a Si:CA ratio of 1:2.5 (Fig. 1(b)), the composite with a Si:CA ratio of 1:2.5 exhibits the most uniform dispersion of CA-modified Si nanoparticles. This improvement is attributed to the optimized hydrogen bonding interactions between CA molecules and silicon nanoparticle surface, which help stabilize the nanoparticles and prevent aggregation. The enhanced dispersion leads to a more homogeneous structure, thereby improving the electrochemical performance of the composite. Additionally, the capacity contribution from C-CA@c-ZIF is relatively low (Fig. S4), indicating that while C-CA@c-ZIF contributes to the overall structural stability, the primary capacity is delivered by the silicon.

To investigate the lithium storage behavior of Si@C-CA@c-ZIF anode, electrochemical kinetic analysis was conducted *via* CV at varying scan rates (Fig. 4(a)). The peak current (i) exhibits a power-law relationship with the scan rate (v), expressed as $\lg(i) = \lg(a) + b \lg(v)$ [36]. The diffusion-controlled and capacitive contributions to the electrochemical behavior can be distinguished by the b value. The b value approaching 1.0 indicates a surface-controlled mechanism predominantly influenced by capacitive behavior and rapid kinetics [37]. From the i–v relationship, the fitted b values for peaks 1 and 2 are determined to be 0.737 and 0.741, respectively (Fig. 4(b)). These relatively high b values suggest that the lithium storage capacity of the Si@C-CA@c-ZIF anode is primarily governed by capacitive processes with fast charge-transfer kinetics. The current at a fixed potential (V) can be deconvoluted into capacitive-controlled (k_1v) and diffusion-controlled ($k_2v^{1/2}$) components, described by the equation: $i = k_1v + k_2v^{1/2}$ [38]. By quantifying k_1 and k_2, the contribution of each process at a specific scan rate can be assessed. Following the determination of k_1 and k_2, the contributions from each behavior at specific scan rates can be quantified (Fig. 4(c)). At 0.8 $mV \cdot s^{-1}$, the capacitive contribution of Si@C-CA@c-ZIF anode is significantly prominent, accounting for 71% of the total capacity (Fig. 4(d)). Additionally, the lithium-ion diffusion behavior in Si@C-CA@c-ZIF anode was further investigated using the galvanostatic intermittent titration technique (GITT). Fig. 4(e) presents the GITT profiles for the Si@C-CA@c-ZIF and Si@c-ZIF electrodes lacking CA modification. Based on these results and Fick's second law, the Li^+ diffusion coefficient (D_{Li^+}) is determined using the following simplified equation: $D \approx \frac{4L^2}{\pi\tau}\left(\frac{\Delta E_s}{\Delta E_t}\right)^2$. Here, L denotes the diffusion length of Li^+, corresponding to the electrode thickness, while ΔE_t represents the voltage change, and ΔE_s is the voltage variation induced by the pulse. As illustrated in Fig. 4(f), the D_{Li^+} of Si@C-

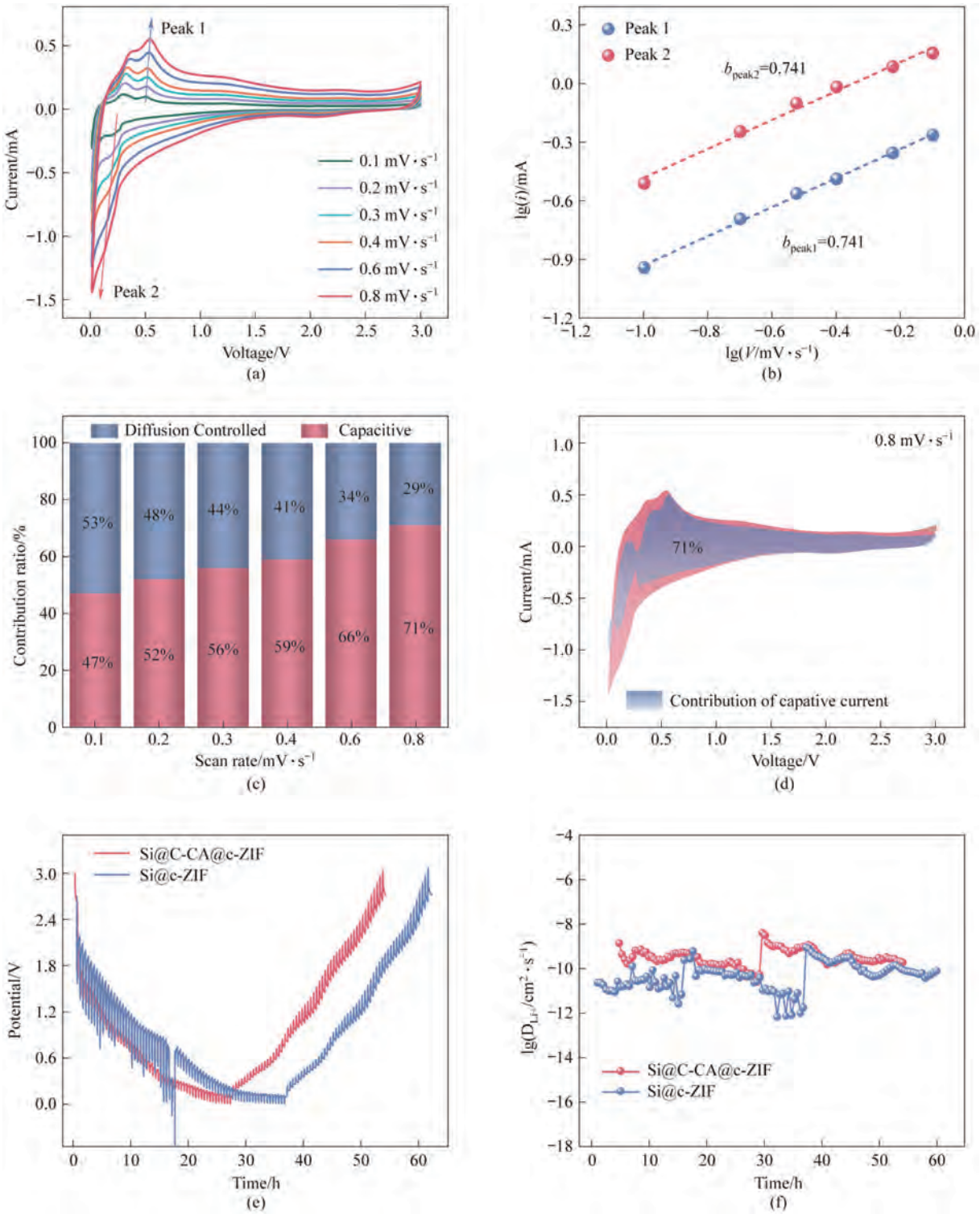

Fig. 4. (a) CV curves of Si@C-CA@c-ZIF anode. (b) Relationship between lg(*i*) and lg(*v*) to determine the *b* value of Si@C-CA@c-ZIF anode. (c) Capacitive and diffusion contributions as functions of scan rate. (d) CV curve and capacitive current contribution at 0.8 $mV \cdot s^{-1}$. (e) GITT potential response curve versus time for Si@C-CA@c-ZIF and Si@c-ZIF anodes. (f) Corresponding plot of Li^+ diffusivity calculated from GITT methods versus potential. Nyquist plots of Si@C-CA@c-ZIF and Si@c-ZIF anodes: (g) before cycling and (h) after cycling. (i) Chart of $\underline{R}_{ct}$ values for the anodes before (striped bars) and after cycling (color-filled bars).

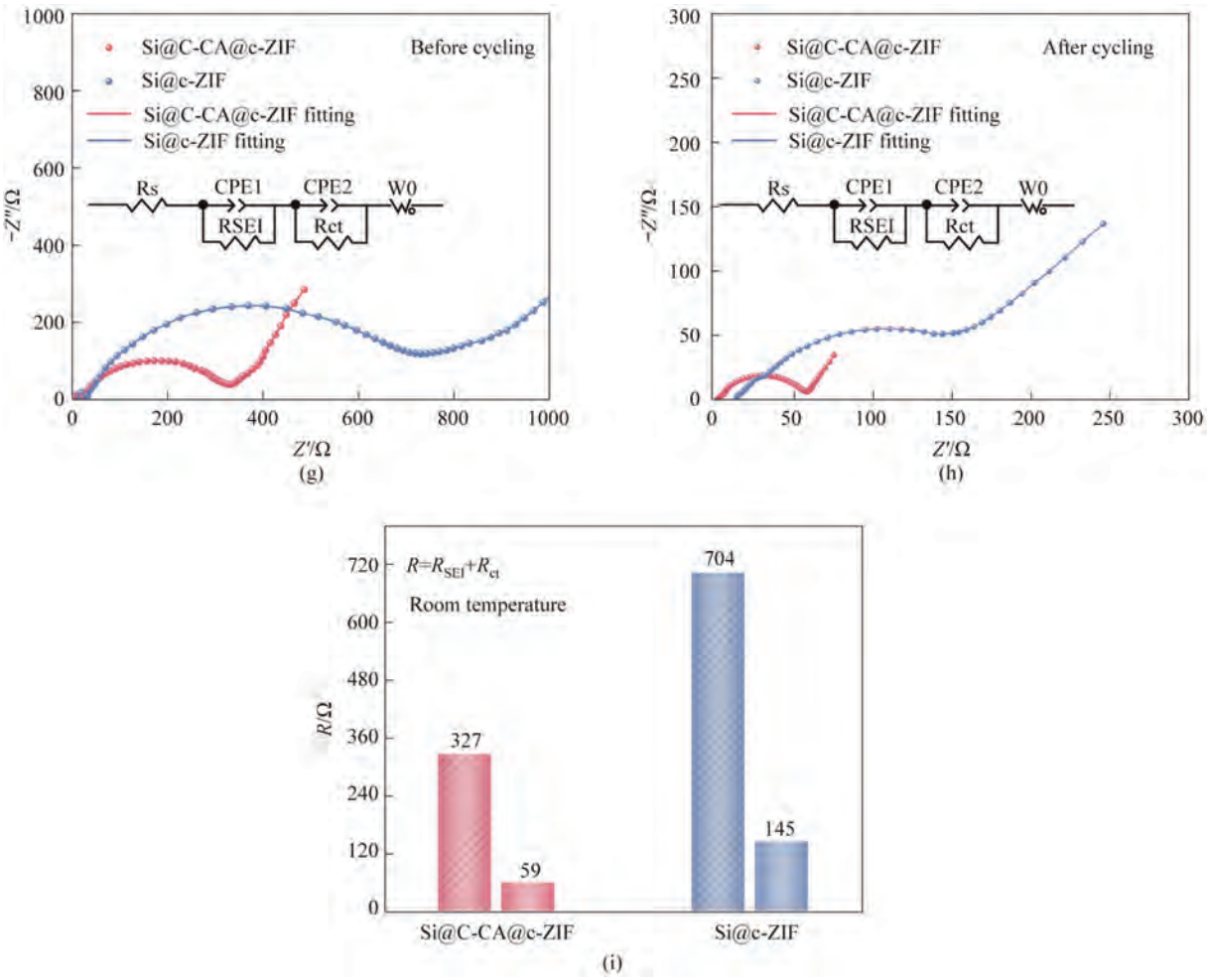

Fig. 4. (*continued*).

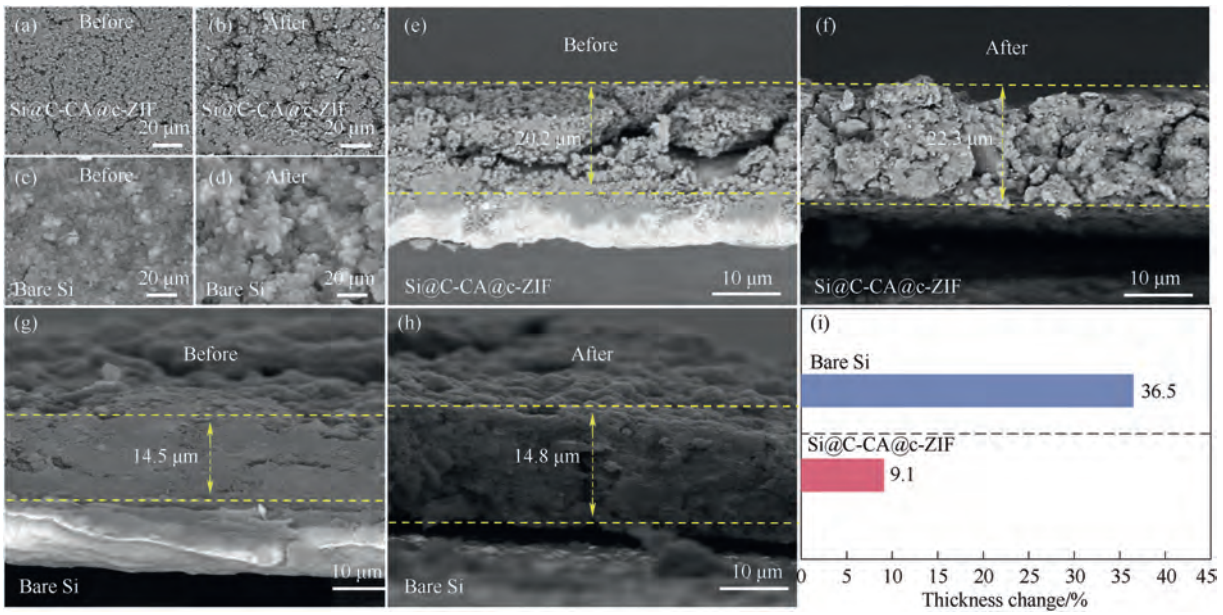

Fig. 5. SEM images of (a, b) Si@C-CA@c-ZIF and (c, d) bare Si anodes before and after 1000 cycles. Cross-sectional of (e, f) Si@C-CA@c-ZIF and (g, h) bare Si anodes before and after 1000 cycles. (i) Corresponding thickness change percentage.

CA@c-ZIF anode exceeds that of the Si@c-ZIF anode without CA modification during both lithiation and delithiation, underscoring the role of CA modification in promoting charge transfer and uniform Li^+ diffusion. To quantify the kinetic enhancement provided by the CA-derived inner carbon layer, electrochemical impedance spectroscopy (EIS) analysis of the Si@C-CA@c-ZIF and Si@c-ZIF anodes was performed both before and after cycling. As illustrated in Fig. 4(g) and (h), the impedance spectra of Si@C-CA@c-ZIF and Si@c-ZIF anodes exhibit two distinct semicircles in both the high-frequency and mid-frequency regions. These semicircles are attributed to the resistance of solid electrolyte interphase (R_{SEI}) and charge transfer resistance (R_{ct}) at the electrode-electrolyte interface, respectively. As illustrated in Fig. 4(i), the resistance of Si@C-CA@c-ZIF anode before cycling (327 Ω) and after cycling (59 Ω) are significantly lower than those of the Si@c-ZIF anode (704 Ω and 145 Ω, respectively). Furthermore, the Si@C-CA@c-ZIF anode exhibits an overall steeper slope in its impedance plot, which confirm the improved ionic and electronic transport properties of Si@C-CA@c-ZIF anode due to the accommodation of volume expansion in Si anode and the enhanced electrical conductivity by the CA-derived amorphous carbon layer.

To elucidate the impact of dual carbon stress-buffering structure on mitigating volume expansion and enhancing structural integrity, top-view (Fig. 5(a)–(d)) and cross-sectional SEM images (Fig. 5(e)–(h)) were used to analyze the anodes before and after cycling. The Si@C-CA@c-ZIF anode exhibits preserved structural integrity (from 20.2 to 22.3 μm) post-cycling, whereas the bare Si anode displays significant surface irregularities (from 14.5 to 19.3 μm) due to stress from excessive volume changes and inadequate interparticle connections, demonstrating a higher expansion rate of 36.5% than that (10.4%) of Si@C-CA@c-ZIF anode. The results indicate that the dual carbon buffering by the inner CA and outer ZIF-67 layers significantly enhances the structural integrity of the electrode, thereby improving cycling stability. To further evaluate the robustness and volume expansion mitigation capabilities of the dual carbon structure, the lithiated Si@C-CA@c-ZIF anode was characterized using SEM and TEM after 1000 cycles. SEM images confirmed the preservation of the polyhedral morphology (Fig. S6(a and b)). Moreover, TEM analysis corroborated the retention of the crystalline Si phase and the presence of Co particles on the graphitic carbon layers derived from ZIF-67 (Fig. S6(c and d)), consistent with the observed mechanical stability of Si@C-CA@c-ZIF anode. Clear lattice fringes with an interplanar spacing of 0.202 nm and 0.335 nm are ascribed to the (1 1 1) plane of Co and the (0 0 2) plane of graphitic carbon layers derived from ZIF-67, respectively [13]. The energy-dispersive X-ray spectroscopy (EDS) mapping of Si@C-CA@c-ZIF anode after 1000 cycles, presented in Fig. S7, demonstrates that Si is uniformly encapsulated within the inner carbon layer, while Co nanoparticles are surrounded by graphitic carbon layers.

4. Conclusions

In summary, a dual carbon protection strategy was proposed to fabricate Si@C-CA@c-ZIF composite by two-step coating and calcination technique. The outer carbon framework was derived from ZIF-67, which encapsulated CA-derived inner carbon-coated Si nanoparticles. Specifically, CA not only promoted a uniform deposition of ZIF-67 on the Si surface but acted as an inner carbon precursor, enhancing conductivity while mitigating volumetric expansion of the anode. The ZIF-67-derived outer carbon layer further constrained the expansion of Si particles and improved the overall electrode conductivity. As results, the Si@C-CA@c-ZIF anode exhibited the high specific capacity is high to 924 $mA \cdot h \cdot g^{-1}$ at 1.0 $A \cdot g^{-1}$ after 10 cycles of activation, and it still maintained a reversible capacity of 703.3 $mA \cdot h \cdot g^{-1}$ after 1000 cycles, with a capacity retention rate of 76.1%. The outstanding cycling stability was mainly attributed to the cooperative protection of the dual carbon layers. In particular, the CA-derived carbon layer not only alleviates the stress generated by silicon during the charging and discharge process, and enhances the transport of electrons and ions between silicon and ZIF-67-derived carbon.

CRediT Authorship Contribution Statement

Qianqian Fan: Writing – original draft, Data curation, Software, Project administration. Jing Wang: Methodology, Investigation, Formal analysis. Zhiyuan Gao: Software, Formal analysis. Zhenpeng Zhu: Data curation, Writing – review & editing. Xingmei Guo: Writing – review & editing. Yuanjun Liu: Methodology, Software. Xiangjun Zheng: Investigation, Data curation. Zhongyao Duan: Software. Qinghong Kong: Writing – review & editing, Resources. Junhao Zhang: Supervision, Project administration, Funding acquisition.

Declaration of Competing Interest

The authors declare that they have no known competing financial interests or personal relationships that could have appeared to influence the work reported in this paper.

Acknowledgements

The work was financially supported by Industry foresight and common key technology research in Carbon Peak and Carbon Neutrality Special Project from Zhenjiang city (CG2023003), National Natural Science Foundation of China (22379056, 22409076).

Supplementary Material

Supplementary data to this article can be found online at https://doi.org/10.1016/j.cjche.2025.06.012.

References

[1] L.Q. Mai, M.Y. Yan, Y.L. Zhao, Track batteries degrading in real time, *Nature* 546 (7659) (2017) 469–470.
[2] H. Gu, M.Y. Gao, K. Shen, T.L. Zhang, J.H. Zhang, X.J. Zheng, X.M. Guo, Y.J. Liu, F. Cao, H.X. Gu, Q.H. Kong, S.L. Xiong, F127 assisted fabrication of Ge/rGO/CNTs nanocomposites with three-dimensional network structure for efficient lithium storage, *Chin. Chem. Lett.* 35 (9) (2024) 109273.
[3] Q.Q. Fan, J.H. Zhang, S.Y. Fan, B.J. Xi, Z.Y. Gao, X.M. Guo, Z.Y. Duan, X.J. Zheng, Y.J. Liu, S.L. Xiong, Advances in functional organosulfur-based mediators for regulating performance of lithium metal batteries, *Adv. Mater.* 36 (45) (2024) e2409521.
[4] L. Sun, Y. Liu, L.J. Wang, Z. Jin, Advances and future prospects of micro-silicon anodes for high-energy-density lithium-ion batteries: a comprehensive review, *Adv. Funct. Mater.* 34 (39) (2024) 2403032.
[5] J. Choi, H. Jeong, J. Jang, A.R. Jeon, I. Kang, M. Kwon, J. Hong, M. Lee, Weakly solvating solution enables chemical prelithiation of graphite-SiO_x anodes for high-energy Li-ion batteries, *J. Am. Chem. Soc.* 143 (24) (2021) 9169–9176.
[6] H. Gu, Z.P. Zhu, Z.Y. Gao, J.H. Zhang, X.M. Guo, Y.J. Liu, X.J. Zheng, Q.Q. Fan, Z. Y. Duan, F. Cao, C.S. Li, Q.H. Kong, J. University, Ge–Si/C nanofiber composite with enhanced cyclic stability and rate capability for lithium-ion batteries, *ACS Appl. Nano Mater.* 8 (5) (2025) 2196–2204.
[7] J.L. Chen, X.M. Guo, M.Y. Gao, J. Wang, S.Q. Sun, K. Xue, S.Y. Zhang, Y.J. Liu, J.H. Zhang, Self-supporting dual-confined porous Si@c-ZIF@carbon nanofibers for high-performance lithium-ion batteries, *Chem. Commun.* 57 (81) (2021) 10580–10583.
[8] H.T. Xia, X.J. Mu, J.H. Zhou, W.P. Liu, G.J. Wu, F. Dang, D.M. Zhang, L. Miao, H. Q. Qin, Z.J. Zhang, X.X. Lei, A.J. Lu, Z.X. Mo, Realization of high-capacity coulombic efficiency in sodium alginate/carbon nanotube double network coated Si-anode for lithium-ion batteries, *Sustain. Mater. Technol.* 40 (2024) e00940.
[9] P.L. Yu, Z.W. Li, D.C. Zhang, Q. Xiong, J. Yu, C.Y. Zhi, Hierarchical yolk-shell silicon/carbon anode materials enhanced by vertical graphene sheets for

commercial lithium-ion battery applications, *Adv. Funct. Mater.* 35 (2) (2025) 2413081.
[10] Z.Y. He, C.X. Zhang, Z.X. Zhu, Y.X. Yu, C. Zheng, F. Wei, Advances in carbon nanotubes and carbon coatings as conductive networks in silicon-based anodes, *Adv. Funct. Mater.* 34 (48) (2024) 2408285.
[11] S.Y. Zhang, Y.C. Xue, Y.T. Zhang, C.X. Zhu, X.M. Guo, F. Cao, X.J. Zheng, Q.H. Kong, J.H. Zhang, T.X. Fan, KOH-assisted aqueous synthesis of bimetallic metal-organic frameworks and their derived selenide composites for efficient lithium storage, *Int. J. Miner. Metall. Mater.* 30 (4) (2023) 601–610.
[12] K.M. Chen, Z.W. Li, J.H. Zhou, J. Gao, H.Q. Qin, W.P. Liu, X.X. Lei, X.Y. Wang, L. Miao, Hollow nitrogen-doped carbon layer-coated nano-silicon as anode material for high-performance lithium-ion batteries, *Appl. Mater. Today* 42 (2025) 102561.
[13] R.S. Gao, J. Tang, X.L. Yu, S. Tang, K. Ozawa, T. Sasaki, L.C. Qin, *In situ* synthesis of MOF-derived carbon shells for silicon anode with improved lithium-ion storage, *Nano Energy* 70 (2020) 104444.
[14] B.Q. Chen, D.M. Xu, S.M. Chai, Z. Chang, A.Q. Pan, Enhanced silicon anodes with robust SEI formation enabled by functional conductive binder, *Adv. Funct. Mater.* 34 (34) (2024) 2401794.
[15] Q.Q. Wu, Y.T. Zhong, R.M. Chen, G.Y. Ling, X.H. Wang, Y.R. Shen, C. Hao, Cu-Ag-C@Ni3S4 with core shell structure and rose derived carbon electrode materials: an environmentally friendly supercapacitor with high energy and power density, *Ind. Crops Prod.* 222 (2024) 119676.
[16] B.J. Chen, L.H. Zu, Y. Liu, R.J. Meng, Y.T. Feng, C.X. Peng, F. Zhu, T.Z. Hao, J.J. Ru, Y.G. Wang, J.H. Yang, Space-confined atomic clusters catalyze superassembly of silicon nanodots within carbon frameworks for use in lithium-ion batteries, *Angew. Chem., Int. Ed.* 59 (8) (2020) 3137–3142.
[17] Y.Z. Zhou, Y.J. Yang, G.L. Hou, D. Yi, B. Zhou, S.M. Chen, T.D. Lam, F.L. Yuan, D. Golberg, X. Wang, Stress-relieving defects enable ultra-stable silicon anode for Li-ion storage, *Nano Energy* 70 (2020) 104568.
[18] D. Jin, X.F. Yang, Y.Q. Ou, M.M. Rao, Y.T. Zhong, G.M. Zhou, D.Q. Ye, Y.C. Qiu, Y. P. Wu, W.S. Li, Thermal pyrolysis of Si@ZIF-67 into Si@N-doped CNTs towards highly stable lithium storage, *Sci. Bull.* 65 (6) (2020) 452–459.
[19] C.L. Jiang, L. Xiang, S.J. Miao, L. Shi, D.H. Xie, J.X. Yan, Z.J. Zheng, X.M. Zhang, Y. B. Tang, Flexible interface design for stress regulation of a silicon anode toward highly stable dual-ion batteries, *Adv. Mater.* 32 (17) (2020) e1908470.
[20] J.J. Zhao, J. Chen, M.M. Zhou, Q. Zhang, X.C. Li, J.Q. Pan, Ultra-firm phthalocyanine-based tetragonal covalent organic framework layer @ nano silicon anode for high durability Li-ion battery, *Chem. Eng. J.* 488 (2024) 151110.
[21] Y.H. Song, L. Zuo, S.H. Chen, J.F. Wu, H.Q. Hou, L. Wang, Porous nano-Si/carbon derived from zeolitic imidazolate frameworks@nano-Si as anode materials for lithium-ion batteries, *Electrochim. Acta* 173 (2015) 588–594.
[22] Z.Y. Wang, H.H. Zhang, X.Y. Zhang, X.M. Wang, X. Zhang, Solvent-free and large-scale synthesis of SiO_x/C nanocomposite with carbon encapsulation for high-performance lithium-ion battery anodes, *Composites, Part B* 247 (2022) 110308.
[23] T.L. Zhang, M.R. Wu, H. Gu, H.W. Yu, M. Zhou, X.M. Guo, Y.J. Liu, X.J. Zheng, Q. H. Kong, J.H. Zhang, Double carbon modified CoS_2/NiS_2 as anode material for efficient lithium storage performance, *J. Energy Storage* 73 (2023) 108981.
[24] Y.Y. Yu, C. Yang, Y. Jiang, J.D. Zhu, J.H. Zhang, M.J. Jiang, Consecutive covalent bonds reconstruct robust dual-interfaces by carbonized binder to enable conductive-additive-free durable silicon anode, *Nano Energy* 130 (2024) 110108.
[25] X.K. Wang, Y. Pan, X.H. Wang, Y.N. Guo, C.H. Ni, J.B. Wu, C. Hao, High performance hybrid supercapacitors assembled with multi-cavity nickel cobalt sulfide hollow microspheres as cathode and porous typha-derived carbon as anode, *Ind. Crops Prod.* 189 (2022) 115863.
[26] H. Chen, Y.Y. Xiong, J. Li, J. Abed, D. Wang, A. Pedrazo-Tardajos, Y.P. Cao, Y.T. Zhang, Y. Wang, M. Shakouri, Q.F. Xiao, Y.F. Hu, S. Bals, E.H. Sargent, C.Y. Su, Z. Y. Yang, Epitaxially grown silicon-based single-atom catalyst for visible-light-driven syngas production, *Nat. Commun.* 14 (1) (2023) 1719.
[27] J. Ma, J. Yu, G.Y. Chen, Y. Bai, S.K. Liu, Y.G. Hu, M. Al-Mamun, Y. Wang, W.B. Gong, D. Liu, Y.F. Li, R. Long, H.J. Zhao, Y.J. Xiong, Rational design of N-doped carbon-coated cobalt nanoparticles for highly efficient and durable photothermal CO_2 conversion, *Adv. Mater.* 35 (42) (2023) e2302537.
[28] K. Xiao, J. Wang, Z. Chen, Y. Qian, Z. Liu, L. Zhang, X. Chen, J. Liu, X. Fan, Z.X. Shen, Improving polysulfides adsorption and redox kinetics by the Co_4N nanoparticle/N-doped carbon composites for lithium-sulfur batteries, *Small* 15 (25) (2019) e1901454.
[29] F. Yuan, Y.N. Li, Y.Q. Wang, Z.J. Li, Q.J. Wang, H.L. Sun, D. Zhang, W. Wang, B. Wang, Cobalt nanoparticles synergize with oxygen-containing functional groups to realize fast and stable potassium storage for carbon anode, *Adv. Funct. Mater.* 33 (46) (2023) 2304753.
[30] H. Wu, G.H. Yu, L.J. Pan, N. Liu, M.T. McDowell, Z.N. Bao, Y. Cui, Stable Li-ion battery anodes by *in situ* polymerization of conducting hydrogel to conformally coat silicon nanoparticles, *Nat. Commun.* 4 (2013) 1943.
[31] M.Y. Gao, Z.H. Tang, M.R. Wu, J.L. Chen, Y.C. Xue, X.M. Guo, Y.J. Liu, Q.H. Kong, J.H. Zhang, Self-supporting N, P doped Si/CNTs/CNFs composites with fiber network for high-performance lithium-ion batteries, *J. Alloys Compd.* 857 (2021) 157554.
[32] W.W. Zeng, L. Wang, X. Peng, T.F. Liu, Y.Y. Jiang, F. Qin, L. Hu, P.K. Chu, K.F. Huo, Y.H. Zhou, Enhanced ion conductivity in conducting polymer binder for high-performance silicon anodes in advanced lithium-ion batteries, *Adv. Energy Mater.* 8 (11) (2018) 1702314.
[33] L. Wang, Z.H. Wang, L.L. Xie, L.M. Zhu, X.Y. Cao, ZIF-67-derived N-doped Co/C nanocubes as high-performance anode materials for lithium-ion batteries, *ACS Appl. Mater. Interfaces* 11 (18) (2019) 16619–16628.
[34] X.M. Fan, T. Cai, S.Y. Wang, Z.H. Yang, W.X. Zhang, Carbon nanotube-reinforced dual carbon stress-buffering for highly stable silicon anode material in lithium-ion battery, *Small* 19 (30) (2023) e2300431.
[35] Q. Wang, J.C. Su, H.L. Chen, D.Q. Wang, X.Y. Tian, Y.J. Zhang, X. Feng, S. Wang, J. Li, H.L. Jin, Highly conductive nitrogen-doped sp2/sp3 hybrid carbon as a conductor-free charge storage host, *Adv. Funct. Mater.* 32 (51) (2022) 2209201.
[36] M.Y. Gao, Y.C. Xue, Y.T. Zhang, C.X. Zhu, H.W. Yu, X.M. Guo, S.S. Sun, S.L. Xiong, Q.H. Kong, J.H. Zhang, Growing Co–Ni–Se nanosheets on 3D carbon frameworks as advanced dual functional electrodes for supercapacitors and sodium ion batteries, *Inorg. Chem. Front.* 9 (15) (2022) 3933–3942.
[37] J.L. Chen, J. Wang, S.Y. Zhang, K. Xue, J.H. Zhang, F. Cao, Q.H. Kong, X.M. Guo, Si nanoparticles confined in N, P-doped double carbon as efficient anode materials for lithium ion batteries, *J. Alloys Compd.* 935 (2023) 167850.
[38] H.W. Yu, M.Y. Gao, M. Zhou, H. Gu, X.J. Zheng, X.M. Guo, Y.J. Liu, F. Cao, Q.H. Kong, J.H. Zhang, F127/PDA dual-assisted fabricating high dispersed Ge nanoparticles/N-doped porous carbon composites with efficient lithium storage, *J. Mater. Res. Technol.* 26 (2023) 5055–5064.